Journal of Power Sources 196 (2011) 6863–6869

Contents lists available at ScienceDirect

Journal of Power Sources

journal homepage: www.elsevier.com/locate/jpowsour

Carbothermal synthesis of Sn-based composites as negative electrode for lithium-ion batteries

M. Mouyane[a], J.-M. Ruiz[a], M. Artus[b], S. Cassaignon[b], J.-P. Jolivet[b], G. Caillon[c], C. Jordy[c], K. Driesen[d], J. Scoyer[d], L. Stievano[a,*], J. Olivier-Fourcade[a], J.-C. Jumas[a,**]

[a] ICG-AIME (UMR 5253) Université Montpellier II, CC 1502, Place E. Bataillon, 34095 Montpellier Cedex 5, France
[b] LCMCP (UMR 7574), Université Paris VI, Collège de France, Bât. C-D, 11 Place M. Berthelot, 75231 Paris Cedex 05, France
[c] SAFT, Direction de la Recherche, 111-113 Bd Alfred Daney, 33074 Bordeaux, France
[d] UMICORE, Group Research, Kasteelstraat 7, BE2200 Olen, Belgium

ARTICLE INFO

Article history:
Received 3 August 2010
Received in revised form 1 September 2010
Accepted 2 September 2010
Available online 15 September 2010

Keywords:
Sn-based composites
Li-ion batteries
Carbothermal reduction
Anode materials
Mössbauer spectroscopy
Electrochemistry

ABSTRACT

The composite [Sn–BPO_4/xC] to be used as negative electrode material for the storage of electrochemical energy was obtained by dispersing electroactive tin species onto a BPO_4 buffer matrix by carbothermal reduction of a mixture of SnO_2 and nanosized BPO_4. This composite material was thoroughly characterized by X-ray diffraction, Scanning Electron Microscopy, ^{119}Sn Mössbauer spectroscopy and Raman spectroscopy. The electrochemical tests of this new material highlight its very interesting electrochemical properties, i.e., a discharge capacity of 850 mAh g^{-1} for the first cycle and reversible capacity around 585 mAh g^{-1} at C/5 rate. These electrochemical performances are attributed to the very high dispersion and stabilisation of tin metal particles onto the BPO_4 matrix. The irreversible capacity observed for the first charge/discharge cycle is due the reduction of interfacial Sn^{II} species and to the passivation of the anode surface by liquid electrolyte decomposition (formation of the SEI layer).

1. Introduction

In the last 20 years lithium-ion batteries have known a tremendous growth in the field of consumer applications such as computers, telecommunication equipment, mobile phone or electric and hybrid vehicles. However, in order to respond to the new demand in emerging fields, such as the development of full electric vehicles which are nowadays one of the main objectives of the car industry, a technological breakthrough is needed in order to improve the volumic and massive storage capacity of batteries as well as their cycling life. In the case of negative electrode materials, graphite is currently employed as the anode electrode material, even though it provides only a limited theoretical capacity (372 mAh g^{-1}) [1].

On the other hand, Sn has a much larger theoretical capacity (990 mAh g^{-1}, corresponding to the formation of the lithium-rich alloy $Li_{22}Sn_5$ [2]) and thus Sn-based materials have been suggested as a promising alternative to graphite-based electrode materials [3]. However the large volume expansion during lithiation and de-lithiation causes structural instability, resulting in poor cyclic performances [4]. This problem can be solved by dispersing small tin metal particles onto an electrochemically inactive matrix able to buffer the volume expansion assuring the electric conductivity of the material upon cycling [5]. Previous studies have shown that the dispersion of tin on a BPO_4 matrix improves noticeably the reversible cycling behavior compared to pure tin metal [6,7]. Further improvements can be obtained by optimizing the dispersion method of Sn in the matrix.

In the present study, the preparation of a new Sn–BPO_4/xC composite material by carbothermal synthesis, leading to highly dispersed metallic tin particles onto the BPO_4 buffer matrix is presented. The carbothermal synthesis was first tested starting from mixtures of SnO_2 and carbon black (molar ratio C:Sn = 2) in the absence of BPO_4, producing a Sn/xC powder composite which was then used as references. The carbothermal reaction can be written as follows:

$$SnO_2 + (2-x)C \rightarrow Sn + (2-2x)CO + xCO_2$$

where x varies between 0 and 1 depending upon the reaction conditions and in particular the reaction atmosphere. The remaining unreacted carbon, corresponding to a molar fraction of x per mole of tin, is also an important constituent of the composite, improv-

* Corresponding author. Tel.: +33 467143346; fax: +33 467143304.
** Corresponding author. Tel. +33 467143309; fax: +33 467143304.
E-mail addresses: lorenzo.stievano@univ-montp2.fr (L. Stievano), jean-claude.jumas@univ-montp2.fr (J.-C. Jumas).

0378-7753/$ – see front matter © 2010 Elsevier B.V. All rights reserved.
doi:10.1016/j.jpowsour.2010.09.001

Table 1
^{119}Sn Mössbauer hyperfine parameters at room temperature for the Sn/*x*C and Sn–$(BPO_4)_{0.2}$/*x*C composites. Isomer shifts are given relative to the reference $BaSnO_3$.

Samples	Tin species	δ (mm s^{-1})	Δ (mm s^{-1})	2Γ (mm s^{-1})	S.F. (%)	E.F. (%)
Sn/*x*C	Sn^0	2.53(2)	0.22(3)	0.92(2)	92(2)	99
	Sn^{IV}	−0.01(5)	0.55(6)	0.69(12)	8(2)	1
Sn-$(BPO_4)_{0.2}$/*x*C	Sn^0	2.56(1)	0.27(3)	0.84(3)	69(2)	79
	Sn^{II}	3.21(2)	1.81(3)	0.83(4)	31(4)	21

ing its electrical conductivity and its cohesion. The best synthesis conditions were obtained under argon flow. These conditions were thus used for the synthesis in the presence of BPO_4 to give the final Sn–BPO_4/*x*C composite, allowing an intimate mixing of the metal and the matrix.

These composites were studied by X-ray diffraction (XRD), scanning electron microscopy (SEM), chemical analysis and ^{119}Sn Mössbauer spectroscopy (TMS). The ^{119}Sn Mössbauer spectra obtained at room temperature for the pristine materials after the carbothermal process show the formation of highly dispersed Sn particles. Moreover, the Sn–BPO_4/*x*C composite electrode exhibits a high electrochemical capacity together with relatively stable cycling performances, showing to be an interesting candidate for the possible application in lithium-ion accumulators.

2. Experimental

2.1. Materials

The synthesis of the BPO_4 matrix was performed using an improved version of the sol–gel method of Moffat and Neeleman [8], starting from a mixture of phosphoric acid (H_3PO_4) and tri isopropyl borate ($(C_3H_7O)_3B$), with a molar ratio of 1:1. The solution was heated at 70 °C under vacuum in order to remove the alcohol formed (propanol) and thus shift the equilibrium toward the formation of BPO_4 until the powder inside the balloon was fully dried.

The composite materials Sn/*x*C and Sn–BPO_4/*x*C (without and with BPO_4, respectively), were synthesized by solid state reaction (carbothermal process). Appropriate mixtures of SnO_2 (Umicore), carbon black and BPO_4 (molar ratios: C:Sn = 2; BPO_4:Sn = 0.2) were mechanically ground to ensure the thorough mixing of the starting materials, and put into vitreous carbon vessels which were then placed inside a horizontal tube furnace heated at 1000 °C. The mixtures were heated for 3 h in a constant flow of argon and rapidly quenched to room temperature after removing the vessel from the furnace. The samples were then gently ground to powder in an agate mortar, giving black powders.

2.2. Methods

The crystalline phases of the as-synthesized composite were analyzed by X-ray diffraction (XRD) using a Philips Gonio diffractometer. XRD patterns were recorded in the Bragg–Brentano θ–2θ continuous mode using the CuK_α radiation (λ = 1.5418 Å). Structural refinements were carried out using the Rietveld method with the WinplotR/Fullprof package [9,10].

^{119}Sn transmission Mössbauer spectra (TMS) were recorded with both source and absorber at room temperature in the constant acceleration mode using components manufactured by ORTEC and WISSEL and a source of $Ca^{119m}SnO_3$ with a nominal activity of 370 MBq. The velocity scale was calibrated with the magnetically split sextet spectrum of a high-purity α-Fe foil as the reference absorber, using a ^{57}Co(Rh) source. The spectra were fitted by appropriate combinations of Lorentzian profiles by the least-squares method using the ISOfit program [11], and the goodness of fits was controlled by a classical χ^2 test. Hyperfine parameters such as isomer shift (δ), quadrupole splitting (Δ), relative resonance area of the sub-spectra (S.F.) and effective molar fractions (E.F.) calculated taking into account the Lamb–Mössbauer factors of the observed tin species are reported in Table 1. All isomer shifts are given with respect to the room temperature spectrum of $BaSnO_3$.

Table 2
Spectral parameters obtained by the deconvolution of the Ramans spectra of carbon black and of the two Sn/*x*C and Sn-$(BPO_4)_{0.2}$/*x*C composites.

Sample		Carbon black	Sn/*x*C	Sn–$(BPO_4)_{0.2}$/*x*C
Component position	A_{1g}	1331(2)	1327(2)	1327(2)
	E_{2g}	1583(2)	1581(2)	1575(2)
	E'_{2g}	1617(2)	1613(2)	1607(2)
	d	1166(6)	1211(4)	1184(3)
	g	1545(10)	1550(6)	1533(8)
Relative intensity	A_{1g}	59(1)	65(1)	63(1)
	E_{2g}	15(2)	11(1)	11(1)
	E'_{2g}	14(2)	11(1)	12(1)
	d	1(1)	4(1)	3(1)
	g	10(2)	9(2)	11(2)
D/G ratio		2.0	2.9	2.7

The morphology of the as-synthesized composite was revealed by scanning electron microscopy (SEM, JEOL JSM-6300F, field emission electron microscope).

The carbon content of the as-made samples was determined using a CHN analyzer Carlo-Erba NA 1500.

Raman scattering experiments were performed over the spectral range of 100–3800 cm^{-1} for all compositions using a Raman microscope Jobin–Yvon HORIBA with the Ar ion laser line at 473 nm. The laser power was set to approximately 50 mW to avoid thermal damage to the samples. The Raman spectra were deconvoluted into single Voigt profile components using the computer program PeakFit (Jandel Scientific Software, 1998). The result of the fit is summarized in Table 2.

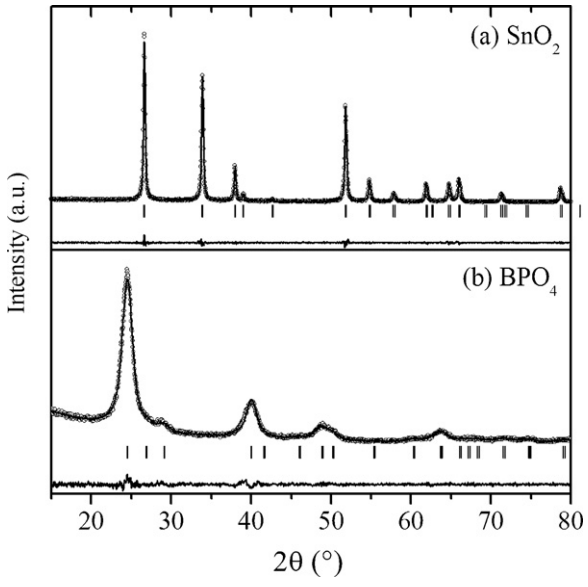

Fig. 1. X-ray powder diffraction patterns for: (a) SnO_2 and (b) BPO_4.

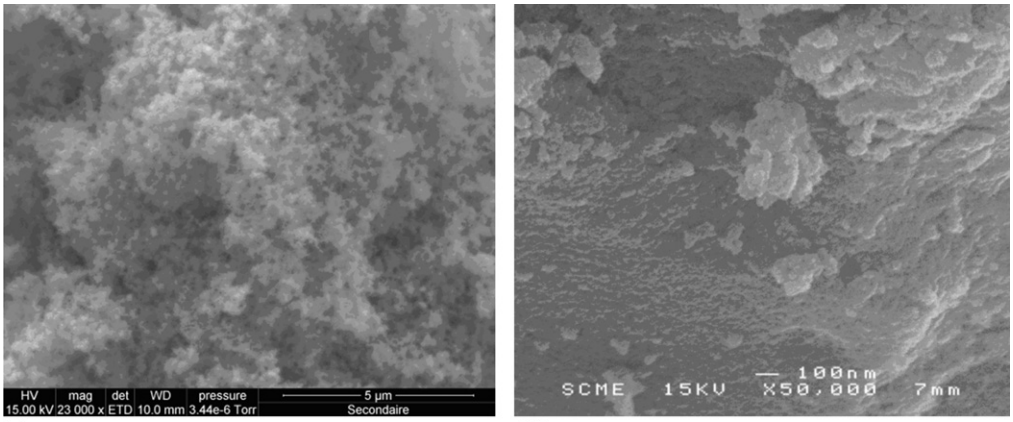

Fig. 2. Scanning electron microscopy images of the starting compounds: (a) SnO_2 and (b) BPO_4.

Electrochemical test were carried out in Swagelok™ two-electrode cells. The working electrodes were prepared as pellets by pressing a mixture of the 80 wt.% active material, 10 wt.% polytetrafluoroethylene (PTFE) binder and 10 wt.% carbon black to assure acceptable mechanical cohesion and electric conductivity. A lithium foil was used as the negative electrode. The electrolyte consisted of 1 M $LiPF_6$ in 1:1:3 in vol. ratio mixture of propylene carbonate (PC)/ethyl carbonate (EC)/dimethyl carbonate (DMC), and Whatman paper (borosilicate glass microfibre filters) was used as separator. The cell was assembled in an Ar-filled glove box. The discharge–charge tests were carried out by means of a Mac Pile II automated system in galvanostatic mode, in a constant current density between 0.01 and 1.2 V vs. Li^+/Li^0 at C/5 rate, equivalent to specific rate of 38 mA g^{-1} (C/*n* expresses the reaction of 1 mole of Li^+ per mole of active material, i.e., the whole composite, in *n* hours).

3. Results and discussion

3.1. Starting materials

The XRD patterns of the pristine SnO_2 and of the freshly synthesized BPO_4, are shown in Fig. 1a and b, respectively. All diffraction peaks in Fig. 1a can be attributed to the tetragonal SnO_2 phase with the space group $P4_2/mnm$ (JCPDS file #770448). The SnO_2 patterns show high crystallinity and the lattice parameters ($a = b = 473.68(3)$ pm, $c = 318.60(2)$ pm) are in good agreement with those reported by Gondal and Drmosh [12]. Finally, the analysis of the diffraction profiles with the usual Debye–Scherrer model provides a crystallite size of about 50 nm.

In Fig. 1b, all reflections can be attributed to the tetragonal BPO_4 phase with the space group I-4 (JCPDS file #791467). The pattern of this phase shows broad peaks due to the small size of the crystallites. The lattice parameters ($a = b = 433.7(1)$ pm, $c = 663.4(2)$ pm) are in good agreement with the data reported in the literature [13]. In this case, the application of the Debye–Scherrer formula gives a crystallite size of about 3 nm.

The morphology of the compounds analyzed by SEM is shown in Fig. 2. In the case of SnO_2, nanoparticles with an average size of about 50 nm form larger agglomerates, in good agreement with the grain size measured by XRD. For BPO_4, large agglomerates of nanoparticles with sizes between 10 and 30 nm are observed. In this case, the presence of agglomerates of nanoparticles with small crystalline domaine sizes agrees well with the XRD results.

The room temperature ^{119}Sn Mössbauer spectrum of pristine SnO_2 (not shown) can be fitted to a narrow unresolved quadrupole doublet with an isomer shift of $-0.01(1)$ mm s^{-1} and a quadrupole splitting of $0.51(1)$ mm s^{-1}, respectively. These hyperfine parameters agree perfectly with those typically observed for SnO_2 [14].

3.2. Sn/xC composite

The carbothermal synthesis of the Sn/*x*C composite produced a black powder. Fig. 3 shows the diffraction peaks of the XRD pattern of the as prepared sample. All diffraction peaks can be attributed to the tetragonal β-Sn phase, whereas no peaks attributable to SnO_2 are observed. The lattice parameters $a = b = 583.03(2)$ pm and $c = 318.11(1)$ pm correspond to the typical values found in the literature for β-Sn metal [15]. The formation of crystalline β-Sn at the expenses of SnO_2 is the sign of a successful carbothermal synthesis. Moreover, chemical analysis indicates that the amount of carbon in the final Sn/*x*C composite is about 7%. Since no peak attributable to carbon phases is observed in the diffraction pattern, all the carbon remaining in the sample is amorphous.

The microstructure of the composite Sn/*x*C obtained by carbothermal reduction of SnO_2 investigated by SEM (Fig. 4) shows, in agreement with XRD, the presence of homogeneous spherical tin-metal particles with sizes smaller than 5 µm decorated with carbon particles. The presence of carbon on the surface of the tin metal is confirmed by EDX and electron diffraction analysis on several single metal particles (not shown).

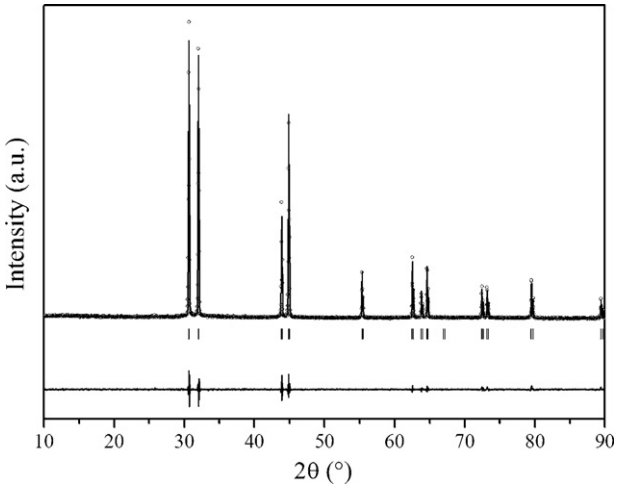

Fig. 3. X-ray powder diffraction patterns of Sn/*x*C composite.

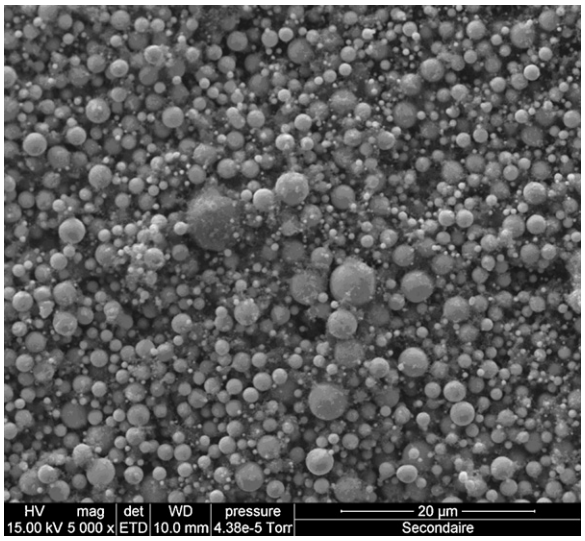

Fig. 4. Scanning electron microscopy representation of the Sn/*x*C composite.

Fig. 5 shows the ^{119}Sn transmission Mössbauer spectrum of Sn/*x*C composite measured at room temperature. The spectrum can be fitted to two spectral components (Table 1): the main component, a narrow quadrupole doublet with an isomer shift of 2.53(2) mm s^{-1} and a quadrupole splitting of 0.22(3) mm s^{-1}, corresponds to β-Sn metal [3,16] and agrees well with the XRD results (Fig. 3). The second sub-spectrum, with isomer shift and quadrupole splitting of −0.01(5) and 0.55(6) mm s^{-1}, respectively, corresponds to a small fraction of the starting SnO_2 which was not completely reduced. The effective atomic fraction of SnO_2 (Table 1), determined by using the Lamb–Mössbauer factors of the two observed species ($f(Sn^0) = 0.07$ [6] and $f(SnO_2) = 0.56$ [17]) is only 1% of the total tin, and is thus not observed in both SEM and XRD.

The Raman spectra of carbon reference used in carbothermal synthesis and of Sn/*x*C composite are shown in Fig. 6a and b, respectively. The same bands are observed in the spectra of both samples with some slight differences in positions and intensities (cf. Table 2). The D band observed at 1330 cm^{-1} corresponds to the A_{1g} vibrational mode [18] and can be attributed to the infinite extension of sp^3 bonded carbon (diamond-like) [19]. The G band observed at about 1600 cm^{-1} can be deconvoluted into two sub-components: the E_{2g} vibrational mode at 1580 cm^{-1} is related to the sp^2 bonded carbon (graphite), whereas the E'_{2g} band at 1620 cm^{-1} is related to symmetry breaking sp^2 bonded carbon and interstitial default [19]. The large and diffuse d and g bands located at

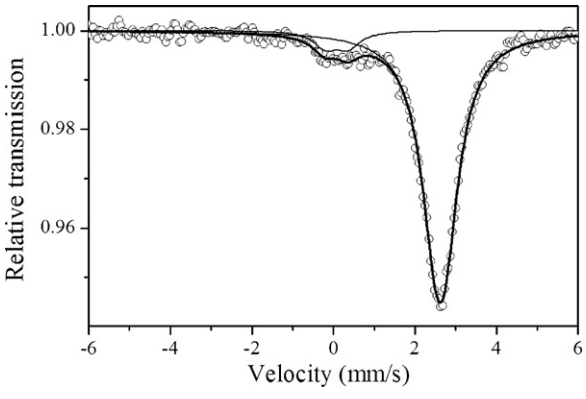

Fig. 5. Room temperature ^{119}Sn Mössbauer spectrum of the reference Sn/*x*C composite.

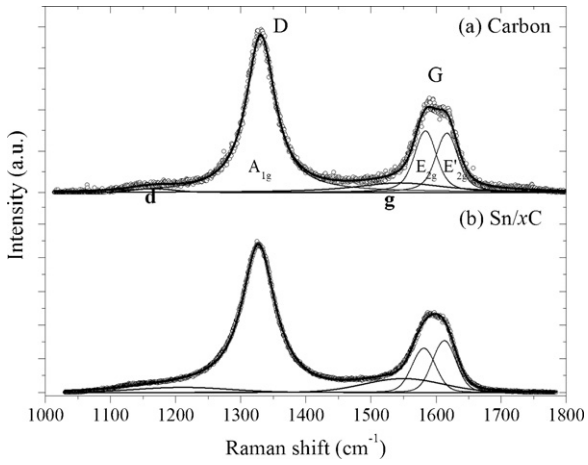

Fig. 6. Raman spectra of carbon black (a) and of the Sn/*x*C composite (b).

about 1200 and 1550 cm^{-1}, respectively, correspond to broaden and overlapped sp^2 and sp^3 bonded carbon, and are often observed in amorphous carbonaceous materials [18].

The relative intensity of the D band versus G band (D:G intensity ratio) is attributed to increased carbon disorder. The band width of the D and G bands is relatively narrow and very similar in both samples, indicating that highly crystalline regions with very small dimensions (undetected by XRD) exist in both samples. However, for the Sn/*x*C composite, a slight decrease of the D:G ratio is observed together with an increase in intensity of the D and G bands. These observations reflect an increase of the relative amount of amorphous carbon in the composite sample after carbothermal reaction. These results agree well with the presence of tin metal particles coated with carbon, as observed by SEM (Fig. 4).

3.3. Sn–BPO_4/*x*C composite

The XRD patterns of the Sn–BPO_4/*x*C composite obtained after annealing of the mixture of BPO_4, C and SnO_2 are shown in Fig. 7. Only the peaks of crystalline β-Sn (tetragonal system, lattice parameters $a = b = 5.83.21(4)$ pm and $c = 318.22(2)$ pm) can be identified in the diffraction pattern, together with a broad scattering peak between 10° and 18°, corresponding to the formation of an amorphous phase [20]. These results show that the complete reaction of the starting SnO_2 goes along with the complete amorphisation of the BPO_4 matrix.

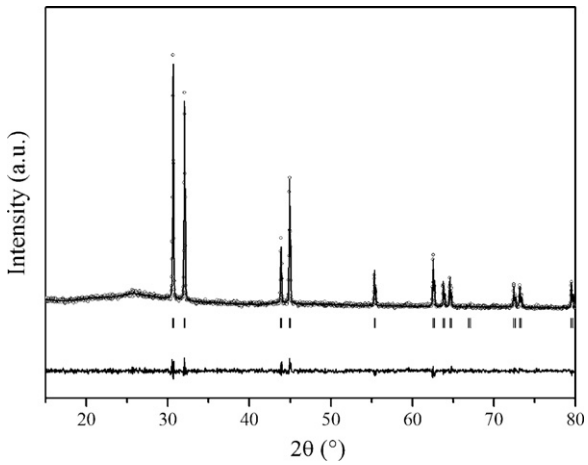

Fig. 7. X-ray powder diffraction pattern of the Sn–BPO_4/*x*C composite.

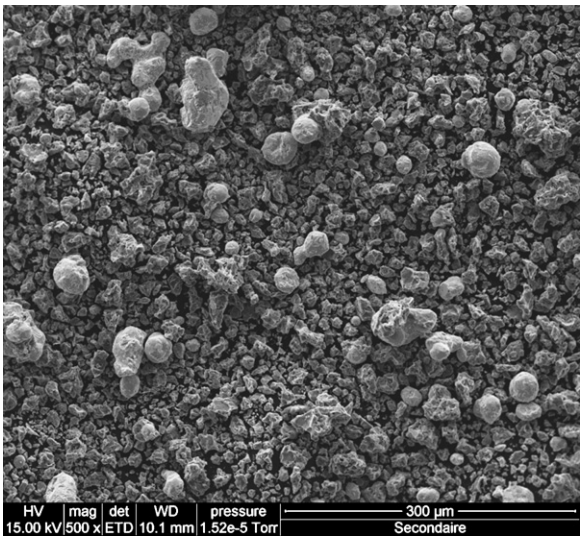

Fig. 8. Scanning electron microscopy representation of the Sn–BPO_4/*x*C composite.

Chemical analysis shows that the carbon proportion in the Sn–BPO_4/xC composite is about 7%, i.e. practically the same amount previously observed for the Sn/xC composite. The morphology of the Sn–BPO_4/xC composite observed by SEM (Fig. 8) is rather inhomogeneous, with particle sizes varying largely between 5 and 70 μm.

The room temperature Mössbauer spectrum of the Sn–BPO_4/*x*C composite, shown in Fig. 9, can be decomposed into two quadrupole doublets: the main doublet, with a relative intensity of 69%, has hyperfine parameters typical of tin metal (Table 1), in agreement with previous data [3,16] and with the XRD results (Fig. 7). The second doublet has parameters typical of divalent tin (Table 1), very similar to those of Sn^{II} species in a borophosphate glasses with composition $SnB_{0.6}P_{0.4}O_{2.9}$ [21]. Taking into account the relative Lamb–Mössbauer factors of these two species previously determined in reference [6] ($f(Sn^0) = 0.07$ and $f(Sn^{II}) = 0.12$ [6]), one obtains a relative abundance of 21% of Sn^{II} (Table 1) which is now included in the amorphous matrix. The presence of divalent tin species in an amorphous phase, which can be explained by the reaction of the newly formed Sn^0 with the BPO_4 matrix in the presence of traces of water and/or oxygen, is commonly observed in this kind of Sn-based composites and is usually attributed to divalent tin species formed at the interface between the tin metal particles and the BPO_4 matrix [6,7,20,22–24].

The Raman spectrum for the Sn–BPO_4/*x*C composite, shown in Fig. 10, allows one to verify the impact of carbothermal reaction in the presence of BPO_4 on the nature of the remaining carbon. The spectrum of the composite is very similar to that of the reference composite Sn/*x*C, with practically the same position and intensity of the different bands, the same D:G ratio and the same intensity of the d and g bands (cf. Table 2). This result suggests that the presence of BPO_4 does not influence noticeably the reactivity of the carbon, and that the carbon remaining in the two composites after the carbothermal reaction, with or without BPO_4, is nearly the same.

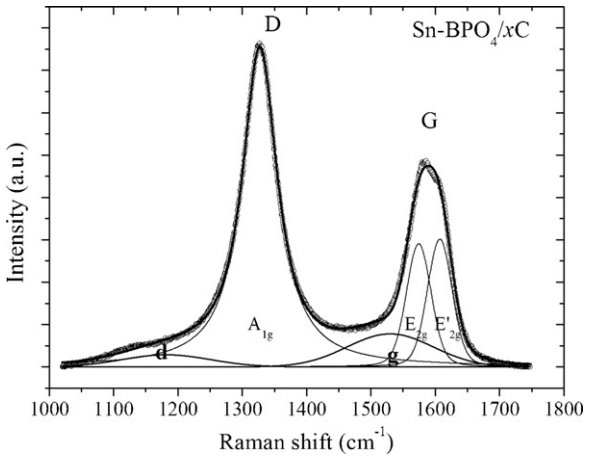

Fig. 10. Raman spectrum of the Sn–BPO_4/*x*C composite.

The global picture resulting from this characterization is that the composite results from the intimate mixture of tin metal particles in contact with an amorphous matrix containing a relatively important amount of divalent tin.

3.4. Electrochemical properties of the Sn–BPO_4/xC composite

The galvanostatic response against lithium metal of the Sn–BPO_4/*x*C composite electrode recorded between 0.01 and 1.2 V vs. Li^+/Li^0 at C/5 rate is shown in Fig. 11 together with the electrochemical cycling of the reference composite Sn/*x*C obtained without BPO_4. In the case of the Sn–BPO_4/*x*C composite, only the first three discharge/charge cycles are shown for the sake of clarity.

During the first discharge process of Sn–BPO_4/*x*C, the reaction with lithium starts at 1.59 V vs. Li^+/Li^0, with the apparition of a small plateau. This process corresponds to reduction of divalent tin, which is extruded from the amorphous matrix to form tin metal

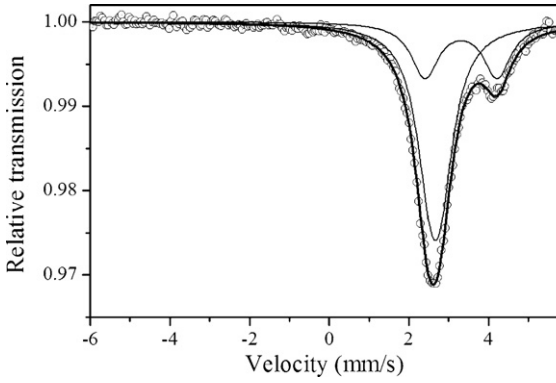

Fig. 9. Room temperature ^{119}Sn Mössbauer spectrum of the Sn–BPO_4/*x*C composite.

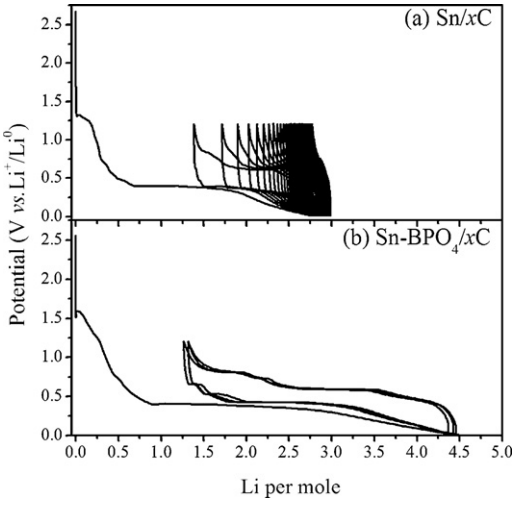

Fig. 11. Galvanostatic discharge/charge curves of Sn/*x*C (a) and Sn–BPO_4/*x*C (b) against Li metal at C/5 rate.

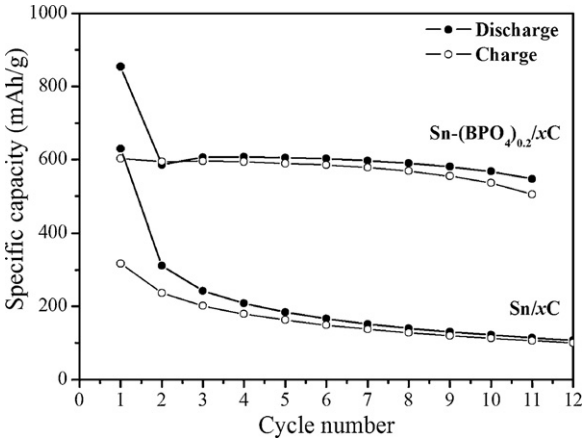

Fig. 12. Discharge/charge capacity of the Sn/*x*C and Sn–BPO_4/*x*C composites as function of the cycle number.

[20]. At the end of this process, the discharge voltage drops to 0.8 V vs. Li^+/Li^0, where the formation of the solid electrolyte interphase (SEI) accompanies the irreversible reduction of the electrolyte on the surface of the carbon particles [25]. A long plateau appears at about 0.9 reacted Li per Sn–BPO_4/*x*C formula unit at 0.40 V vs. Li^+/Li^0 which extends on for about 2 reacted Li corresponding to a formation of a sequence of Li_xSn alloys. After this long the voltage decreased gradually until 0.01 V vs. Li^+/Li^0. The same processes are observed in the case of Sn/*x*C, except for the reduction plateau of divalent tin, which is absent in this case, and for the much more rapid voltage drop after the plateau of formation of the Li_xSn alloys.

The first charge process of the Sn–BPO_4/*x*C composite exhibits three distinct plateaus at 0.6 V, 0.7 V and 0.8 vs. Li^+/Li^0 corresponding to the formation of reversible Li_xSn alloys, in agreement with the theoretical potential values of the literature [26]. In the following cycles, the formations of these plateaus are reversible which indicates the good electrochemical behavior of the material electrode. The same plateaus, only much shorter in length and decreasing rapidly upon cycling, are observed for the reference Sn/*x*C composite.

The total capacity (reversible plus irreversible) resulting from the first discharge is of 854 and 630 mAh g^{-1} for Sn–BPO_4/*x*C and Sn/*x*C, respectively. The first charge process evidences relatively large irreversible capacities in both cases. In the case Sn/*x*C, the observed irreversible capacity of 313 mAh g^{-1}, corresponding to 50% of the reacted Li, reminds that usually observed for SnO_2-based materials. In the latter case, however, the irreversible capacity is mainly due to the amount of Li used for reducing the Sn^{IV} to tin metal, whereas in the case of Sn/*x*C such a big loss can be mainly ascribed to the bad conductivity and/or reactivity of the Sn–Li alloys formed after the first cycle. In fact, the formation of Sn–Li alloys during the first discharge starts already at about 0.5 reacted Li, and only about two third of these alloys is transformed back into tin metal during the charge process.

In the case of Sn–BPO_4/*x*C, an irreversible capacity of 252 mAh g^{-1} is observed, corresponding to 29% of the reacted Li. This value practically corresponds almost only to the Li consumed for reducing the interfacial Sn^{II} to tin metal and to the formation of the SEI layer. In fact, the first charge goes back to about 1.2 reacted Li, roughly at the beginning of the formation of Li–Sn alloy during the first discharge, indicating that almost all of the tin alloys formed during the first discharge with the Li are electrochemically active during the charge process.

Moreover, an additional important difference between the two samples is the capacity retention upon cycling, shown in Fig. 12. In fact, while the capacity of the Sn/*x*C material fades dramatically in the first three cycles, similarly to pure tin electrode materials, a capacity between 550 and 600 mAh g^{-1} in both charge and discharge is retained for Sn–BPO_4/*x*C for at least 10 cycles.These results confirm that the carbothermal synthesis assures an intimate dispersion of tin on the BPO_4 matrix, verified by the good cycling behavior of the Sn–BPO_4/*x*C, and are thus encouraging, even though further improvements are necessary, especially in the cycling behavior, for a possible application of these materials in real batteries.

4. Conclusions

A new Sn-based composite material (Sn–BPO_4/*x*C) with a capacity of 550 mAh g^{-1} stable for at least 11 cycles was obtained by carbothermal synthesis. This method allowed an intimate mixing of the metal formed in situ, its matrix and residual carbon. These results highlight the important role of the BPO_4 matrix (among others) in maintaining the dispersion of the active species and in buffering the volume variation during cycling. These results show that the capacity of tin-based composites can be improved sensibly if a carbothermal method is used for their synthesis. Further improvements might also be obtained from an appropriate formulation.

Acknowledgments

This work is carried out in the framework of the national project ANECDOTE (ANR-07-Stock-E-03-02). The authors express their sincere gratitude to the "Agence Nationale de la Recherche" and to the DERBI, EUREKA and AEROSPACE VALLEY competitiveness poles for financial supports. Région Languedoc-Roussillon is also acknowledged for the support to the "Grand Plateau Technique Réseau des Rayons X et γ" (contracts nos. 06-8856-01 and 06-8856-02). Belgian authors thank IWT for financial support.

References

[1] J.C. Chang, Y.F. Tzeng, J.M. Chen, H.T. Chiu, C.Y. Lee, Electrochim. Acta 54 (2009) 7066–7070.
[2] W.H. Pu, X.M. He, J.G. Ren, C.R. Wan, C.Y. Jiang, Electrochim. Acta 50 (2005) 4140–4145.
[3] F. Robert, P.E. Lippens, J. Olivier-Foureade, J.C. Jumas, F. Gillot, M. Morcrette, J.M. Tarascon, J. Solid State Chem. 180 (2007) 339–348.
[4] L.Y. Beaulieu, K.W. Eberman, R.L. Turner, L.J. Krause, J.R. Dahn, Electrochem. Solid State Lett. 4 (2001) A137–A140.
[5] J. C. Jumas, F. Robert, P. E. Lippens, J. Olivier-Fourcade, P. Willmann, Patent N FR287385 (2004), EP1794828 2007.
[6] D.E. Conte, A. Aboulaich, F. Robert, J. Olivier-Fourcade, J.C. Jumas, C. Jordy, P. Willmann, J. Solid State Chem. 183 (2010) 65–75.
[7] A. Aboulaich, M. Mouyane, F. Robert, P.E. Lippens, J. Olivier-Fourcade, P. Willmann, J.C. Jumas, J. Power Sources 174 (2007) 1224–1228.
[8] J.B. Moffat, J.F. Neeleman, J. Catal. 31 (1973) 274–277.
[9] J. Rodríguez-Carvajal, Phys. B: Condens. Matter 193 (1993) 55–69.
[10] T. Roisnel, J. Rodriguez-Carvajal, Mater. Sci. Forum 378–381 (2001) 118–123.
[11] W. Kündig, Nucl. Instrum. Methods 75 (1969) 336–340.
[12] M.A. Gondal, Q.A. Drmosh, T.A. Saleh, Appl. Surf. Sci. 256 (2010) 7067–7070.
[13] G.E.R. Schulze, Zeitschrift Fur Physikalische Chemie-Abteilung B-Chemie Der Elementarprozesse Aufbau Der Materie 24 (1934) 215–240.
[14] I. Sandu, T. Brousse, D.M. Schleich, M. Danot, J. Solid State Chem. 177 (2004) 4332–4340.
[15] J.A. Lee, G.V. Raynor, Proc. Phys. Soc. Lond. Sec. B 67 (1954) 737–747.
[16] J.G. Stevens, V.E. Stevens, Ed. Mössbauer Effect Data Center, Mössbauer handbookseries, UNCA, Asheville (NC, USA) Tin-119, 1990.
[17] G.S. Collins, T. Kachnowski, N. Benczerkoller, M. Pasternak, Phys. Rev. B 19 (1979) 1369–1373.
[18] F. Tuinstra, J.L. Koenig, J. Chem. Phys. 53 (1970) 1126–1130.
[19] Y. Wang, D.C. Alsmeyer, R.L. McCreery, Chem. Mater. 2 (1990) 557–563.
[20] A. Aboulaich, F. Robert, P.E. Lippens, L. Aldon, J. Olivier-Fourcade, P. Willmann, J.C. Jumas, Hyperfine Interact. 167 (2006) 733–738.
[21] J. Chouvin, C.P. Vicente, J. Olivier-Fourcade, J.C. Jumas, B. Simon, P. Biensan, Solid State Sci. 6 (2004) 39–46.
[22] F. Robert, F. Morato, J. Chouvin, L. Aldon, P.-E. Lippens, J. Olivier-Fourcade, J.-C. Jumas, B. Simon, P. Biensan, J. Power Sources 119–121 (2003) 581–584.

[23] Z. Edfouf, M.J. Aragon, B. Leon, C.P. Vicente, J.L. Tirado, J. Phys. Chem. C 113 (2009) 5316–5323.
[24] A. Aboulaich, M. Womes, J. Olivier-Fourcade, P. Willmann, J.-C. Jumas, Solid State Sci. 12 (2010) 65–72.
[25] H. Kim, B. Park, H.J. Sohn, T. Kang, J. Power Sources 90 (2000) 59–63.
[26] P.E. Lippens, L. Aldon, C.M. Ionica, F. Robert, J. Olivier-Fourcade, J.C. Jumas, Solid State Ionics-2004, in: P. Knauth, C. Masquelier, E. Traversa, E.D. Wachsman (Eds.) Solid state Ionics-2004, Materials Research Society Symposium Proceeding, Materials Research Society, Warrendale, 2005, p. 249.